

# Chapter 1

## Live Observations of Catalysts Using High-Pressure Scanning Probe Microscopy

Joost Frenken and Irene Groot

**Abstract** Recently it has become clear that essential discrepancies exist between the behavior of catalysts under industrial conditions and the (ultra)high vacuum conditions of traditional laboratory experiments. Differences in structure, composition, reaction mechanism, activity, and selectivity have been observed. These differences indicated the presence of the “pressure gap”, and made it clear that meaningful results can only be obtained at high pressures and temperatures. This chapter focuses on the development of scanning probe microscopy for *operando* observations of active model catalysts. We have developed instrumentation that combines an ultrahigh vacuum environment for model catalyst preparation and characterization with a high-pressure flow reactor cell, integrated with either a scanning tunneling microscope or an atomic force microscope. We combine the structural observations obtained under high-pressure, high-temperature conditions with time-resolved mass spectrometry measurements on the gas mixture leaving the reactor. In this way, we can correlate structural changes of the catalyst due to the gas composition with its catalytic performance. This chapter provides an overview of the instruments we developed and illustrates their performance with results obtained for different model catalysts and reactions.

---

J. Frenken · I. Groot (✉)  
Huygens–Kamerlingh Onnes Laboratory, Leiden University,  
P.O. Box 9504, 2300 RA Leiden, The Netherlands  
e-mail: i.m.n.groot@lic.leidenuniv.nl

J. Frenken  
e-mail: j.frenken@arcnl.nl

J. Frenken  
Advanced Research Center for Nanolithography,  
P.O. Box 93019, 1090 BA Amsterdam, The Netherlands

I. Groot  
Gorlaeus Laboratories, Leiden University,  
P.O. Box 9502, 2300 RA Leiden, The Netherlands

## 1.1 Introduction

The topic of heterogeneous catalysis has been studied extensively in the last one hundred years. Much of our current knowledge has been obtained under conditions that differ significantly from those of practical catalysis. The reason for this discrepancy stems from the fact that most techniques, suitable for obtaining accurate results at the nano-scale, cannot perform under the typical working conditions of industrial catalysis (i.e. high pressures and high temperatures). Surface-sensitive techniques, such as Auger electron spectroscopy (AES), X-ray photoelectron spectroscopy (XPS), or low-energy electron diffraction (LEED), are limited to pressures below  $10^{-5}$  mbar [1]. Although there are cases, where the results obtained at low pressures can be extrapolated to industrial conditions [2, 3], more and more examples exist where this “pressure gap” is found to fundamentally change the reaction mechanisms [4–9]. The pressure gap seems to be the rule, rather than the exception. The investigation of catalysis under more realistic (industrial) conditions, without compromising the sensitivity to the details on the atomic and molecular scale, inescapably forms the next arena in this research field, where major breakthroughs will be forced, both scientifically and in the technological application. But the difference between laboratory studies and chemical industry in terms of pressure and temperature is not the only gap in heterogeneous catalysis research. Also the nature of the catalyst used is very different. In academic studies the catalyst is often simplified to a model system, usually consisting of a single-crystal metal surface, as opposed to industrial catalysts, which generally consist of metal nanoparticles deposited on oxidic, nanoporous supports and are accompanied by additional elements such as promoters, fillers, and binders. This discrepancy is commonly known as the “materials gap”.

### 1.1.1 Why Working Conditions?

Recently it was discovered that reaction mechanisms taking place under typical laboratory conditions of (ultra)high vacuum ( $10^{-5}$ – $10^{-11}$  mbar) can differ significantly from those taking place under high-pressure (HP) conditions (mbar–bar range) [4–9]. Therefore, the last decades have seen a tremendous effort in adapting existing surface-science techniques to high-pressure conditions. One approach is to build a set-up in which ultrahigh vacuum chambers are combined with high-pressure chambers, using differential pumping. With this approach, X-ray photoelectron spectroscopy [10, 11], low-energy ion scattering (LEIS) [12], and transmission electron microscopy (TEM) [13, 14] can operate in the mbar regime. Another approach is the use of micro- or nano-reactors that separate the high-pressure volume from the (ultra)high vacuum part via ultrathin walls of an inert material. Examples are TEM [15] and X-ray microscopy [16].

Some surface-science techniques are able to bridge the pressure gap without facing major limitations, e.g. scanning probe microscopy (SPM) [17–21], sum frequency generation (SFG) laser spectroscopy [22–24], polarization-modulation infrared reflection absorption spectroscopy (PM-IRAS) [25], ultraviolet Raman spectroscopy [26–28], and ellipso-microscopy [29]. Furthermore, the successful application of surface X-ray diffraction (SXRD) [30–32] and X-ray absorption spectroscopy [33, 34] to study catalytic surfaces at high temperatures and pressures was recently published.

Scanning probe microscopy (e.g. scanning tunneling microscopy (STM) and atomic force microscopy (AFM)) is one of the few atomically-sensitive techniques that in principle can operate under conditions varying from millikelvins to temperatures as high as 1000 K [35–37], and pressures varying from  $10^{-11}$  mbar to above 1 bar. These techniques have the possibility to determine the detailed influence of the gas environment on the structure of model catalyst surfaces, to identify active sites for catalytic processes, and to elucidate the role of promoters, all by imaging surfaces with (near)-atomic resolution under the relevant high-pressure, high-temperature conditions of industrial catalysis. There are several practical issues that can affect the quality of the images and the resolution. In addition, when aiming to detect reaction products simultaneously, further complications may arise.

This chapter is organized as follows. We start with a general introduction about STM, followed by a section about the general requirements for the development of SPM instruments that are dedicated to catalysis research under relevant industrial conditions. The chapter concludes with examples of catalytic systems studied using *operando* STM, namely CO oxidation, NO reduction, Fischer-Tropsch synthesis, hydrodesulfurization, and chlorine production.

## 1.2 Scanning Tunneling Microscopy

The scanning tunneling microscope (STM) was invented in 1982 at IBM Zürich by Gerd Binnig and Heinrich Rohrer [38, 39] and implemented by Gerd Binnig, Heinrich Rohrer, Christoph Gerber, and Erich Weibel [40, 41]. The STM was an immediate success, and Binnig and Rohrer were awarded the Noble Prize in Physics in 1986 for their invention. Nowadays, the STM is an indispensable instrument in a physics laboratory, and it is also employed regularly in surface-science and catalysis research.

The main components of an STM consist of [35, 42]:

- An atomically sharp tip. STM tips are usually made from W, Au, or PtIr wire. They are fabricated by cutting or etching the metal wire. *In situ* treatments consist of annealing and sputtering.
- A scanner to raster the tip over the sample surface. This is done by using piezoelectric ceramics, as they can convert electric signals of 1 mV to 1 kV into mechanical motion in the range of fractions of an Å to a few μm.

- A coarse positioning system to choose the region that is to be imaged, to bring the tip within tunneling distance of the sample, and to retract it a few mm when e.g. placing and removing the sample in/from the STM.
- Vibration isolation. For stable operation of the STM, the influence of external vibrations on the tip-sample distance should be minimized, e.g. to 0.01 Å or less. Vibration isolation is usually achieved by suspending the inner STM stage, including tip and sample, by springs, often in combination with a damping system, for example employing eddy currents. In addition, STM setups are often isolated as a whole from external vibrations, for example by use of passive or active isolator legs.
- Feedback electronics to control the tip-sample distance.
- A computer system to control the tip position, to acquire data, and to convert the data into an STM image.

The working principle of an STM is based on the quantum mechanical phenomenon of tunneling: the penetration of electrons through a potential barrier. When the sharp tip of the microscope is placed close enough to the sample surface (5–10 Å), the wave function(s) of the atom(s) at the end of the tip will overlap with the wave functions of the atoms in the sample surface. When a bias voltage is applied between the tip and sample, a tunneling current will flow through the tip-sample gap. Figure 1.1 shows a schematic diagram of the electron energies on the side of the sample and those on the side of the tip, involved in the tunneling process. The tunneling current is given by the following equation:

$$I(d) \propto eV \exp(-\kappa d), \quad (1.1)$$

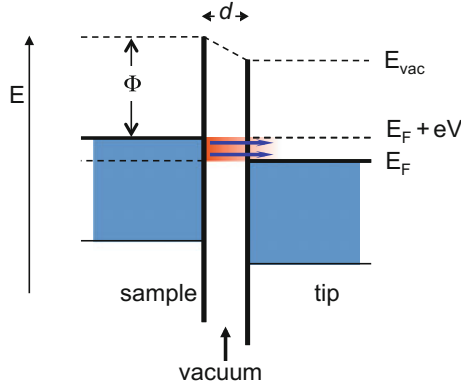


**Fig. 1.1** Schematic energy diagram for the sample and the tip in an STM experiment.  $d$  is the tip-sample distance,  $\Phi$  the work function, which we have chosen identical here for sample and tip,  $E_{vac}$  is the vacuum level and  $E_F$  the Fermi level. The applied bias voltage  $V$  offsets the Fermi levels of the sample and the tip by an energy  $eV$  and gives rise to a net tunneling current between the two, proportional to  $eV$  and depending exponentially on the distance  $d$  and the height of the tunneling barrier  $\Phi$

where  $I(d)$  is the tunneling current as a function of the tunneling gap,  $V$  is the applied bias voltage,  $\kappa \propto \sqrt{\Phi}$ , where  $\Phi$  is the (average) work function of the sample and the tip, and serves as the effective tunneling barrier height, and  $d$  is the tunneling gap. This description is an approximation, only valid at very low tunneling currents, and in the case of equal work functions for tip and sample [35, 42]. The sharp dependence of the tunneling current on the tip-sample distance determines the extremely high vertical resolution of STM. Typically a change of tip-sample distance of 1 Å results in a change in the tunneling current of nearly an order of magnitude. The lateral resolution is determined by the fact that up to 90% of the tunneling current flows between the “last” atom of the tip and the surface atom closest to it. When scanning the tip along the surface, the local density of states of the surface atoms is probed. When the applied sample bias voltage is negative with respect to the tip, the filled states are probed, and when this applied voltage is positive, the empty states are probed.

Three main modes of STM operation are defined, depending on the variation of the lateral coordinates  $x$  and  $y$ , the height  $z$ , the bias voltage  $V$ , and the tunneling current  $I$ . In the constant current mode,  $I$  and  $V$  are kept constant,  $x$  and  $y$  are varied by scanning the tip over the surface, and  $z$  is measured. This is the most widely used scanning mode. To maintain constant tunneling current, the feedback electronics constantly adjust the vertical position of the tip by varying the feedback voltage on the  $z$ -piezoelectric element. For an electronically homogeneous surface, this essentially means that the tip-sample distance is kept constant. The height variations of the surface are inferred from the variations in the feedback voltage as a function of lateral position  $(x, y)$ . This mode can be used even for very rough or strongly inclined surfaces. The scan speed, however, is limited by the finite response time of the feedback electronics. In the constant height mode,  $z$  and  $V$  are kept constant,  $x$  and  $y$  are again varied by scanning the tip over the surface, and  $I$  is measured as a function of the tip position. In this mode, the feedback electronics is turned off or reduced to a low-frequency response, only to follow the slope and gentle height variations. The higher-frequency signature of the atomic-scale structure is not followed by the tip and is recorded as current variations. Since feedback is not required at this high frequency, this type of scanning can be performed at high speed. However, this mode can only be applied for relatively flat surfaces. In the various scanning tunneling spectroscopy (STS) modes, the voltage  $V$  is varied. Since the tunneling current is determined by summing over electron states in the energy interval determined by the bias voltage, varying this voltage will give information on the local density of states as a function of energy. When probing the electronic properties of a very local area or even a single atom, chemical information about the surface species can be obtained. For an extensive overview of the working principles of STM, see e.g. [35, 42].

### 1.3 High-Pressure SPM Instrumentation

The development of STMs operating at (near)-ambient reaction conditions started as early as 1993, with the pioneering work of McIntyre and co-workers [43]. In their design, the STM is contained in a high-pressure cell, consisting of a 2 L stainless-steel vacuum chamber. Using an infrared spot heater, the sample can be heated to 1400 K under atmospheric pressures. In addition, the system is equipped with a differentially-pumped quadrupole mass spectrometer (QMS), which can be used for gas analysis. A few years after this introduction the design was combined with a UHV chamber. Instead of a QMS, a gas chromatograph (GC) was used for gas analysis [44].

After this successful introduction of high-pressure STM, several other designs have been introduced [19, 45–48]. All these HP-STMs had in common that they include a microscope inside a high-pressure reactor, that is connected to a UHV chamber for sample preparation and characterization using common surface-science techniques such as AES, XPS, and LEED. In our group we have adopted a fundamentally different design concept, the ReactorSTM, in which not the entire microscope, but only the tip and its holder, are contained in the high-pressure environment [17]. The motivation for this radically different design is as follows. To be able to fully explore the effect of surface restructuring of the catalyst on its activity, the reaction rate needs to be measured simultaneously with structural measurements using STM. This can be done by operating the cell that contains the STM as a flow reactor, via analysis of the gas leaving the reactor using a QMS or GC. However, when using a cell large enough to contain the entire microscope, the low conversion rates that should be expected on the small active areas of typical model catalysts make that one can obtain measurable product concentrations only at very low flow rates, which would introduce extremely long response times. Furthermore, large reactors also introduce high probabilities for reactants and reaction products to adsorb on and react with the walls of the reactor. These risks also extend to the components of the STM itself, such as the piezo element. The latest version of the ReactorSTM setup is a versatile instrument that provides atomic resolution under harsh reaction conditions [20].

In addition to high-pressure STMs, some high-pressure AFMs have been developed as well. Again, the simplest approach is to operate a standard AFM in a high-pressure cell [49, 50]. However, this severely limits the operating temperature range and the use of corrosive gases. A more advanced approach separates the high-pressure flow cell from the piezo of the AFM scanner with a membrane. In this way, the AFM can operate up to 423 K and 6 bar in liquid [51], or up to 350 K and 100 bar in supercritical CO<sub>2</sub> [52]. These instruments are limited to contact-mode AFM and, due to long equilibration times, to constant temperature. To be able to perform real catalytic studies, we have developed an AFM [21] based on the same principles as the ReactorSTM [20]. We continue in the next sections with further details on the design and performance of these special STM and AFM set-ups.

### 1.3.1 Requirements for Operando SPM

As mentioned in the previous section, an unconventional design for SPM tools suitable for catalytic studies under reaction conditions has been developed in our group. For the development of both the ReactorSTM [20] and the ReactorAFM [21] the following requirements were taken into account:

- The microscope must be suitable for catalytic studies under realistic conditions, i.e. high pressures (1 bar and beyond) and elevated temperatures (at least 400 K). Under these conditions, the microscope must be capable of imaging the catalytic surface with atomic resolution (STM) or step resolution (AFM) and low drift.
- The set-up must be suitable for *operando* studies, i.e. studies combining the structural information of the catalyst with its activity. For this, the time resolution for measurements of the reaction product needs to be 10 s or better.
- The design of the instrument should prevent chemistry taking place anywhere else than on the catalyst surface. Reactions taking place on the reactor walls or elsewhere will not only hamper the accuracy of activity measurements, but may also corrode components of the microscope.
- Measurements should take place on well-defined model catalysts that are initially atomically clean and highly-ordered. The catalyst surface must not be exposed to air between preparation and characterization under reaction conditions.

As explained in Sect. 1.1.1, an STM or AFM has no intrinsic difficulties working at atmospheric pressures and beyond. Due to the small tip-surface distance no significant interference by the surrounding gas molecules is expected. Effects of elevated temperatures include an increase in thermal drift. Using special materials with low expansion coefficients, these effects can be minimized and stable imaging at temperatures as high as 1300 K can be achieved [53]. However, when combining high temperatures with high pressures difficulties may arise. The piezo element, that is used to actuate the tip, must be kept under its Curie temperature. In vacuum conditions, large temperature differences can be maintained over short distances. In the presence of a gas atmosphere, however, heat transport via the gas renders this challenging. In addition, a large temperature difference between sample and piezo causes a convective flow in the gas atmosphere, resulting in erratic drift in the images. We have circumvented this problem by keeping most of the components of the microscope in vacuum, while the sample is exposed to reaction conditions.

To be able to perform catalytic studies under *operando* conditions, the catalytic surface must be contained inside a reactor volume, that, in addition to housing the microscope, is connected to a means of measuring catalytic activity (either via QMS or GC). To optimize both the time resolution and the sensitivity to changes in the concentrations of reactants and products, the ratio between the surface area of the model catalyst and the volume of the reactor, including the gas line connecting the reactor to the gas analysis system, must be maximized. Since SPM can only be used on flat surfaces or on clusters of nanoparticles on flat supports, we are limited to very

small surface areas. To obtain a high ratio between the active surface area and the reactor volume, the reactor volume must be as small as possible.

Under high-pressure, high-temperature conditions, chemical reactions can take place not only on the surface of the model catalyst, but also on the sides and back face of the sample. Furthermore, chemical reactions can take place on other surfaces exposed to the reactive gases such as the walls of the reactor, the sample holder, and elements of the microscope. These undesired reactions not only influence the outcome of the experiment (e.g. higher reactivity can be observed than if the only reactivity measured would be due to the catalyst), it can also seriously damage the instrument, especially when aggressive reactions are studied. To eliminate these undesired reactions as much as possible, inert materials are chosen for the reactor walls. In addition, we keep as much as possible the elements of the microscope and the side and rear faces of the sample outside the reactor volume.

To prepare well-defined, highly-ordered model catalysts, standard cleaning and preparation procedures are employed. These methods, such as ion sputtering, annealing, physical vapor deposition of metals, and gas exposure, require UHV conditions. Techniques to investigate crystal composition, structure, and ordering, such as LEED, AES, and XPS, can only be employed under UHV conditions. Since the prepared catalyst samples cannot be exposed to air when transferring them to the high-pressure reactor and SPM, a combination of a UHV chamber with the microscope and reactor is necessary.

### 1.3.2 *Design of the ReactorSTM*

Figure 1.2 shows a schematic drawing of the concept of the ReactorSTM, in which all of the above-mentioned design criteria are met [17, 20]. The ReactorSTM integrates a very small flow reactor (0.5 mL) having inert walls with a scanning tunneling microscope. The reactor volume is placed inside a UHV system, used for the preparation and characterization of model catalysts. Two gas lines, one for the inlet of gases, one for the outlet, are connected to the reactor. The inlet line is connected to a gas system which controls the flow, mixing ratio, and pressure of the reactant gases (the gas system will be described in more detail in Sect. 1.3.4). The outlet line is connected to the back pressure controller in the gas system, after it has passed a small chamber housing the QMS for analysis of the reactant and product gases that leave the reactor. The only parts of the microscope that are inside the reactor volume are the tip and tip holder. The reactor is sealed off from the surrounding UHV using two flexible O-rings. The lower O-ring (Viton) separates the reactor from the piezo element, that is used to actuate the motion of the tip. The upper O-ring, consisting of Kalrez (Dupont), a chemically resistant material, is pressed between the sample and upper part of the reactor body, thus sealing off the high pressures inside the reactor from the surrounding UHV environment. The sample can be radiatively heated from the rear (the upper side in Fig. 1.2).



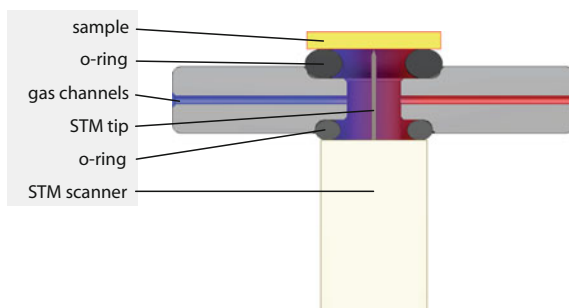


**Fig. 1.2** Conceptual drawing of the ReactorSTM. The STM tip is contained in a small high-pressure volume, while the STM scanner is not exposed to the gases. The sample forms one side of the reactor, while the other walls are chemically inert. Two polymer O-rings seal off the high-pressure volume from the UHV system around it. This figure was reprinted from [20] with permission from the American Institute of Physics

Figures 1.3 and 1.4 show the configuration of the UHV system. It consists of three chambers separated by gate valves. The first chamber is the XPS chamber. Here, the XPS for use under UHV conditions is located. Furthermore, this chamber houses a sample library, and a sample load-lock ensures the loading of samples without breaking the vacuum. The second chamber is the preparation chamber. It contains an ion sputtering gun, a combined LEED/AES system, and an electron-beam evaporator for preparation of metallic nanoparticles. In addition, gas lines with leak valves are present for sample cleaning and catalyst preparation. The third chamber is the STM chamber, which houses the microscope integrated with a small flow reactor. On the top flange of this chamber a seal library has been installed for the Kalrez seals that close off the reactor. Using a wobble stick seals can be placed on and removed from the top plate of the reactor without breaking the vacuum. Sample transfer between the chambers is performed with a rack-and-pinion transfer rod.

In Fig. 1.5 a schematic cross section of the sample holder and the reactor with the microscope is shown. The upper seal consists of a custom-made Kalrez ring (Dupont) that is vulcanized onto a stainless-steel holder, enabling exchange of the seals without breaking the vacuum. Due to the specifications of the Kalrez seal, the operation temperature is limited to 600 K. The STM body is fabricated from Zerodur (Schott), a chemically resistant glass type with low thermal expansion coefficient, minimizing thermal drifting of the STM during temperature changes.

The sample holder is made out of Invar, a low-expansion steel, again to minimize thermal drift. It is strongly pressed against the top of the STM body, making hard mechanical contact via three adjustable screws. In this way, a short and stiff mechanical loop is established between the sample and the tip, which is essential for high-quality imaging. When pressing the sample holder against the STM body, the Kalrez seal is compressed to 80% of its original thickness, providing a leaktight seal. When the reactor is exposed to pressures up to 6 bar, UHV conditions are maintained

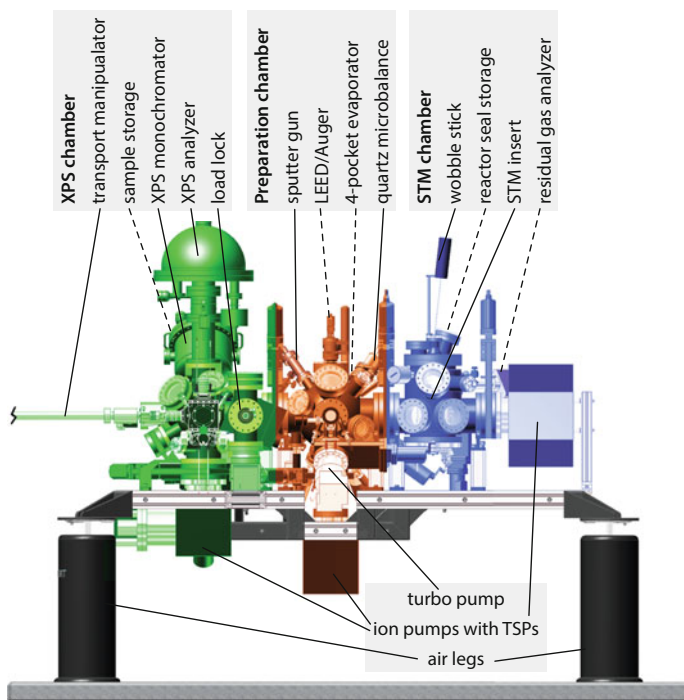


**Fig. 1.3** Schematic drawing of the UHV system showing the three chambers with the equipment for sample preparation and characterization. *Dashed lines* point to components that are not visible. This figure was reprinted from [20] with permission from the American Institute of Physics

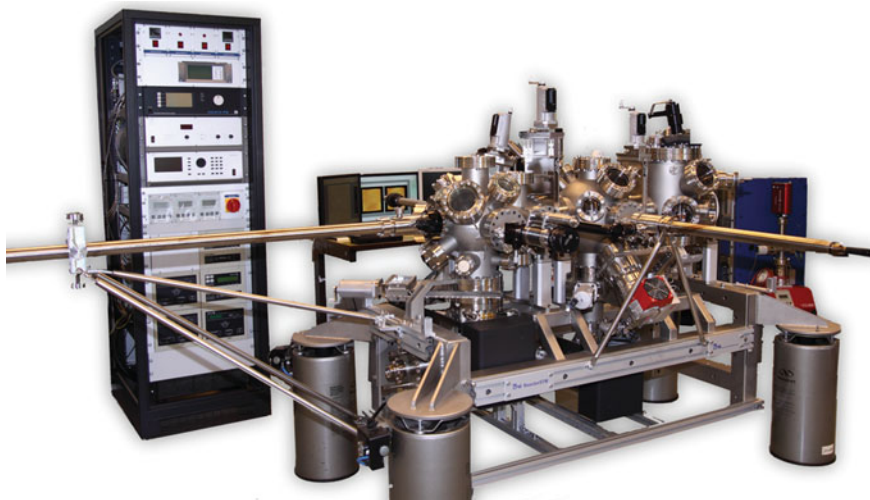


**Fig. 1.4** Photograph of the UHV system showing the chambers with the equipment for sample preparation and characterization. This version does not have the XPS-system incorporated. Photograph courtesy of Leiden Probe Microscopy B.V.

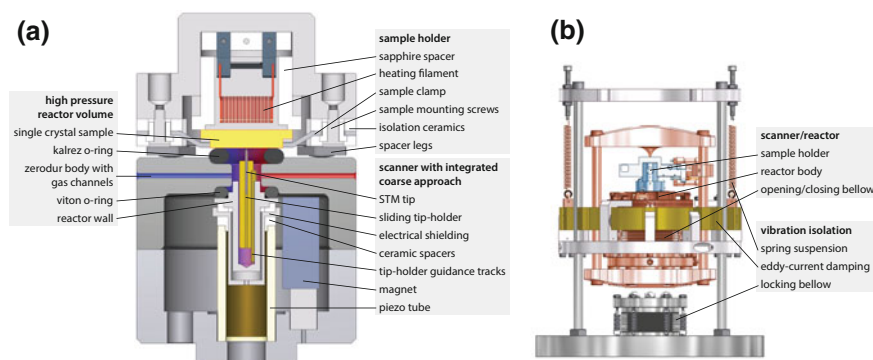
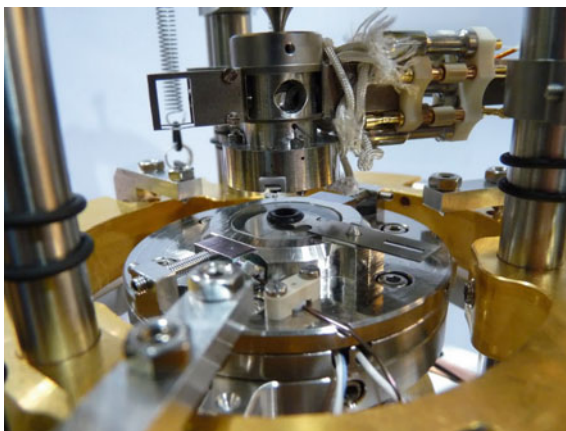


**Fig. 1.5** Detailed schematic of **a** the sample holder, the reactor and the scanner (viewed in cross section), and of **b** the complete STM insert, including its vibration isolation and damping, mounted on a CF-200 flange. This figure was reprinted from [20] with permission from the American Institute of Physics

in its surroundings. The current limitation of 6 bar is due to the gas system, not to the seal. Figure 1.6 shows a photograph of the ReactorSTM assembly with the reactor opened and the sample holder in place.

A single piezo tube (EBL2, EBL Products) is used for both the coarse approach and the fine scanning motion of the tip. The STM tip is clamped in a steel holder, which is pulled against two steel tracks using a SmCo magnet (IBS Magnet). The tip holder and tracks are Au-coated, to ensure chemical inertness and to optimize the stick-slip behavior of the motor. The force of the magnet is determined by its size, shape, and position. It is optimized such, that the maximum acceleration that can be generated along the length axis of the piezo tube is high enough to overcome the static friction force between the tip holder and the tracks. The electrical connec-

**Fig. 1.6** Photograph of the open reactor with the sample holder in place



tion to the tip, necessary to measure the tunneling current, is established via the tip holder, tracks, and the aluminum tube in which the tracks are clamped. An additional aluminum piece provides electrical shielding. The two aluminum parts are electrically isolated from each other and from the piezo tube using two insulating Macor rings (Corning Inc.). The piezo tube is glued to a titanium base, which has a thermal expansion coefficient that compensates the expansion of the piezo tube during temperature changes.

The central STM part, including vibration isolation, eddy current damping, all electrical connections, and the gas capillaries, is mounted on a CF-200 flange (see Fig. 1.5b). Thus, easy insertion of the microscope and reactor into the SPM chamber of the UHV set-up is guaranteed. The STM body that holds the microscope, the reactor, and the sample holder is suspended by a set of springs combined with an eddy current damping system, in order to isolate the STM from external, mechanical vibrations. When transferring samples, the STM body can be locked via controlled inflation of a bellow. A second bellow can be inflated via a thin capillary to press the reactor body to the Kalrez seal, thus closing off the reactor volume from the UHV surroundings. The STM is controlled using fast analog/digital SPM control electronics (Leiden Probe Microscopy B.V.) capable of video-rate STM imaging [54].

### 1.3.3 Design of the ReactorAFM

The instrument described in the previous section, the ReactorSTM, is able to bridge the pressure gap. Scanning tunneling microscopy, however, can only be performed on conductive samples, usually metal single crystals or thin oxide films deposited on metal surfaces. To study metallic nanoparticles deposited onto porous oxide supports, and thereby also bridging the so-called materials gap, a different scanning probe technique is required: the atomic force microscope. While STM uses an electrical current to probe the sample, AFM uses the interaction force between tip and sample, and is therefore independent of its conductivity. To be able to investigate more realistic catalysts, we have developed the ReactorAFM [21]. Its design is based on the proven concept of the ReactorSTM (see Sect. 1.3.2), but its capability to image supported nanoparticles adds unique value for *operando* catalysis research.

The ReactorAFM must be able to resolve nanoparticles supported on flat surfaces under industrially relevant conditions with sufficient detail. The minimum requirements that we have defined are a lateral resolution of 1 nm, and a vertical resolution of 0.1 nm, with a range of at least 1  $\mu\text{m}$  in each direction. Furthermore, the scanner should be sufficiently stable to enable imaging of a single feature on the surface for at least one hour, thus placing constraints on the thermal drift of both the scanner and force sensor. Additional requirements are discussed in Sect. 1.3.1, and most design specifications chosen to meet these requirements are described in Sect. 1.3.2. The AFM scanner, however, differs significantly from the STM scanner. The AFM scanner is based on the piezoelectric read-out of a quartz tuning fork (QTF). Due to the small volume of the reactor, no optical access to the tip is possible, ruling out laser

deflection techniques commonly used in AFM. Since quartz is chemically inert, and exceptionally high resolution has been reported using QTF-based AFM [55, 56], this is the best choice for the ReactorAFM. The high stiffness makes the QTF also relatively insensitive to the presence of the gas atmosphere, thus enabling us in principle to extend imaging with good resolution to reaction conditions.

The QTF with the AFM tip is mounted on a rod that is magnetically clamped inside the piezo tube. Using a stick-slip motion, the rod can slide up and down during the coarse approach of the tip to the sample. The rod consists of two halves and is held against two tracks using a SmCo magnet. The tracks supporting the tip holder are mounted on a capped polyetherimide (PEI) cylinder, located inside the piezo tube. An additional cylinder, made of aluminum, between the PEI component and the piezo tube provides electrical insulation from the high piezo voltages. The PEI cylinder also forms part of the reactor walls, so the piezo tube is not exposed to high-pressure gases. This avoids chemical and thermal stability issues. The two tracks are also used as feedthroughs for the two electrical signals of the QTF through the PEI reactor wall. Each track is in contact with one of the two halves of the tip holder. The tracks traverse the insulating PEI component and are connected by coaxial cables to floating-shield BNC feedthroughs on the CF-200 flange of the insert.

The QTF used is a commercial miniature crystal with a resonance frequency of 32.768 kHz (Micro Crystal AG). The tuning fork is modified to obtain the required overall dimensions of  $1.9 \times 0.5 \times 0.12 \text{ mm}^3$ , and the fundamental resonance frequency is  $\sim 96 \text{ kHz}$ . The QTF is mounted on the tip holder in the QPlus configuration [57], i.e. the lower prong is completely fixed and the upper prong acts as a single piezoelectric cantilever. After fixating the lower prong, the  $Q$ -factor of the first resonance at ambient conditions is  $3 \times 10^3$ . A ceramic spacer is used to tilt the QTF to an angle of  $2.5^\circ$  to ensure that the apex of the upper prong is the first part to come into contact with the sample surface. Figures 1.7 and 1.8 show the resulting assembly.

A micrometer-sized AFM tip is grown at the apex of the upper prong of the QTF, using electron-beam induced deposition (EBID) of platinum employing a scanning electron microscope (SEM). After preparation, the tip consists of 16 atom % platinum, the remainder being amorphous carbon [58]. The electrical connections from the tuning fork electrodes to the tip holder are made by ball bonding using  $25 \text{ }\mu\text{m}$  diameter Au wire. The electrical path continues via the tracks that support the tip holder, followed by coaxial cables to the UHV feedthroughs.

The ReactorAFM operates in non-contact or frequency-modulation (FM) mode. In this mode, the cantilever is oscillated at resonance with an amplitude in the range of 10 pm to 100 nm. When the tip is near the surface, the tip-sample interaction force gradient will influence the effective spring coefficient of the mechanical oscillator, resulting in a shift of the resonance frequency. In the case of dissipative forces, there is also a decrease of the amplitude and an additional phase shift. The resonance frequency is measured by a phase-locked loop. The output signal of this loop is used as the input for the height feedback loop of the AFM scanner in order to trace the surface at constant frequency shift. A separate feedback system adjusts the drive amplitude to keep the oscillation amplitude constant, thereby ensuring that the surface of con-

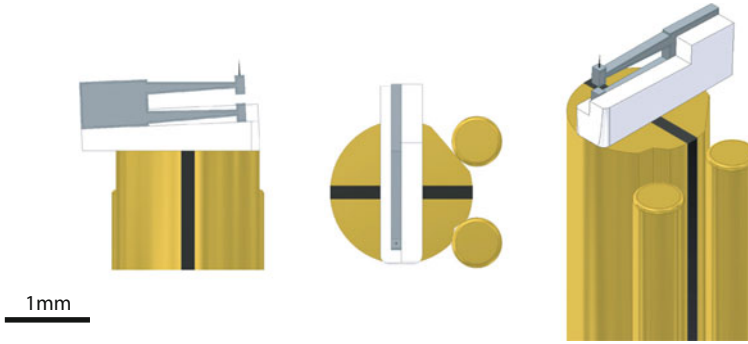


**Fig. 1.7** Three views of the sliding rod with the QTF and the two tracks. The rod consists of two halves, each in contact with one of the two tracks. The slider has a special shape with a groove and a flat side to have a well-defined orientation and thus a well-defined combination of contacts with the two tracks. This figure was reprinted from [21] with permission from the American Institute of Physics

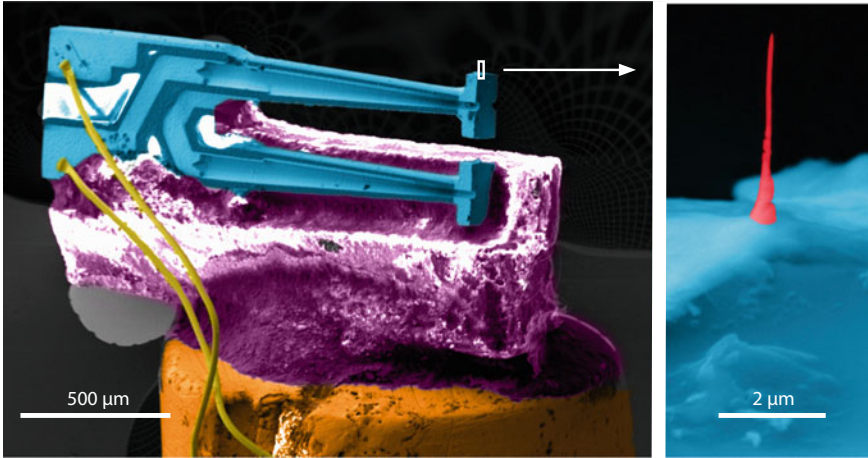


**Fig. 1.8** Scanning electron microscopy images with false colors for enhanced contrast of the QTF glued on a ceramic spacer which is glued to the slider, with a close-up of the apex of the upper prong and the EBID-grown AFM tip. This figure was reprinted from [21] with permission from the American Institute of Physics

stant frequency shift corresponds to a surface of constant force gradient. The drive signal of this amplitude feedback loop is recorded in a separate channel and can be used to derive the dissipative force.

The motion of the QTF is controlled via an excitation/detection circuit located directly outside the UHV system. It is based on a circuit developed by Grober et al., which compensates for the stray capacitance of the QTF, and measures the oscillating current through the QTF with an I-V convertor when it is driven at resonance by an



external oscillator voltage source [59]. The shift in resonance frequency of the QTF is detected using a Zurich Instruments HF2LI lock-in amplifier with phase-locked loop. It also supplies the oscillating drive voltage at resonance. The height feedback and scanning are performed using high-speed SPM electronics from Leiden Probe Microscopy [54].

### 1.3.4 *Design of the Gas System*

To investigate chemical reactions a gas system is required that can mix various gases over wide ranges in composition, with separate control over the gas flow rate of the individual components, and the total pressure in the mixture, and with a response time in the order of a few seconds. This latter requirement necessitates a configuration with small total volume. Furthermore, the system should enable the user to change partial pressures, flow rates, and total pressure without interrupting the imaging. This implies that pressure overshoots, which can cause tip crashes, cannot be tolerated. Finally, one has to recognize that high purity of the gases entering the reactor is essential and that dead volumes or badly refreshed components should be avoided. To separately control the gas composition, flow rate, and total pressure inside the reactor, a combination of mass flow controllers and back pressure controllers (Bronkhorst Hi-Tech) is employed. To choose different pathways for the gases through the gas system, custom-modified versions of GC-valves (Valco) are used. The advantage of these modified valves is that their design allows for complex flow patterns while still keeping the total volume very small and having no dead volume. Figure 1.9 shows an overview of the architecture of the gas manifold as designed by LPM [60]. With this system, up to five different gases can be mixed. The architecture of the rotating valve V1 is such that a gas is either flowing to rotating valve V2 or into the drain/pulse line. In this way, a certain gas flow at a certain pressure set by pressure controller BPC-pulse can be prepared in the drain/pulse line, prior to adding it to the flow through the reactor. In this way, gases can be added to the reactor flow during STM scanning, without any danger for tip crashes. Via RV3, a certain volume of a gas can be dosed to the reactor for gas-titration experiments. To enhance the dynamic range of partial pressures to be set, an additional line with a shunt mass flow controller is installed. To optimize response time, the inner diameter of the gas lines and bores of the valves are chosen to be small, but not too small to prevent unwanted large pressure drops in the system which might compromise the reactor pressure reading. The lines running towards the reactor typically have an inner diameter of 0.5 mm, the lines downstream of the reactor have an inner diameter of 0.75 mm. The gas flow controllers have a capacity up to 10 mL/min (30 mL/min for the carrier gas). Given the volume of the reactor to be 0.5 mL, the refresh rate of the reactor is up to 20 times per minute for a single gas. The response time of the system is determined by the internal volume of the gas manifold and the volume of the gas line connecting the gas manifold to the reactor. Typically it takes 10 seconds after setting up a new gas composition before it ends up at the sample in the reac-

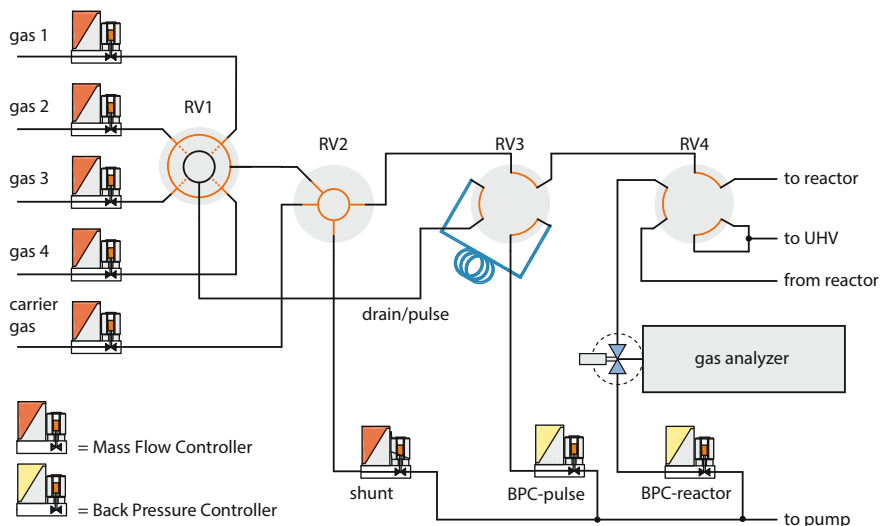


**Fig. 1.9** Manifold for gas mixing and analysis. Up to four reactive gases and a carrier gas can be mixed via a computer-controlled manifold, consisting of rotating valves (RV 1–4), several mass flow controllers, and two back pressure controllers (BPC). A continuous sampling gas analyzer provides high time-resolution gas analysis. This figure was reprinted from [20] with permission from the American Institute of Physics

tor. For the gas manifold used with corrosive gases special materials are employed that can withstand these aggressive conditions (e.g. Hastelloy C gas lines and special polymer seals inside the GC-valves). The gas composition of the outgoing mixture is analyzed using a QMS. All valves of the gas system are operated by a computer. Home-written Labview and Python programs continuously log all valve settings and read-outs of the mass flow and back pressure controllers.

## 1.4 Catalytic Systems Investigated Under High-Pressure Conditions

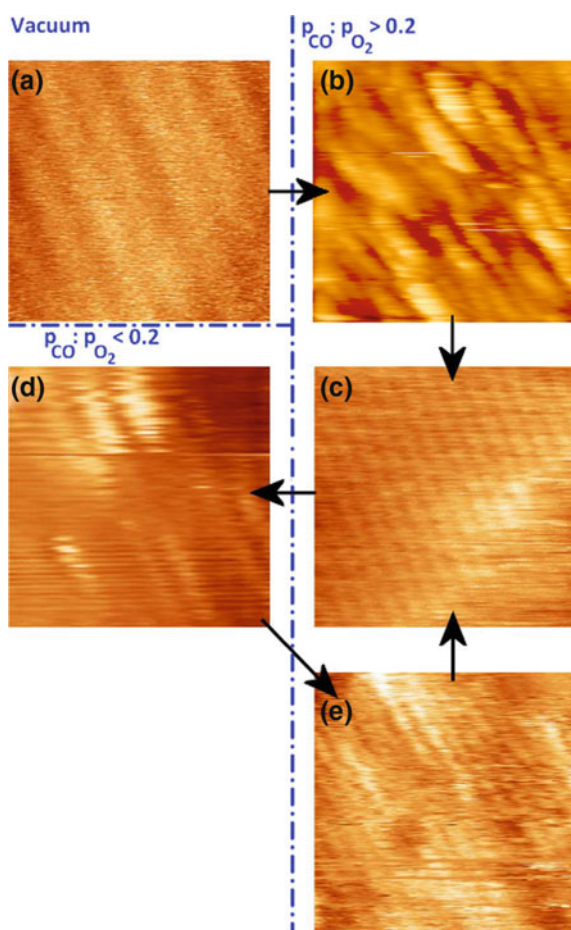
In this section we discuss some catalytic systems that are currently under investigation in our group. We start out with a short summary of effects observed for CO oxidation on Pt(110) and Pd(100). With our ReactorSTM and -AFM setups we have now been able to move beyond this regime of “baby” catalysis toward more relevant reactions and have grown up to study more relevant reactions, such as NO reduction and Fischer-Tropsch synthesis. We complete the overview with first results obtained for two very aggressive systems: the hydrodesulfurization (HDS) reaction and the chlorine production reaction (Deacon process).



### 1.4.1 CO Oxidation on Pt(110)

The first studies performed with the ReactorSTM concerned the prototype reaction of CO oxidation over Pt(110) [6, 61–63]. CO oxidation is one of the reactions taking place in the three-way automotive catalyst [64, 65]. Figure 1.10 shows characteristic STM images for CO oxidation over Pt(110) under reaction conditions [63]. The total pressure in the experiment was 1 bar, and the surface temperature 433 K. Figure 1.10a shows the initial  $(1 \times 2)$  missing-row reconstruction, imaged in vacuum and at room temperature. This reconstruction is well known for Pt(110) under vacuum conditions [66]. When introducing 1 bar of CO in the reactor, and raising the temperature to 433 K, we find initially increased roughness (see Fig. 1.10b), which decays over time, resulting in the flat  $(1 \times 1)$  surface (see Fig. 1.10c). After adding  $O_2$  to the flow in a  $CO:O_2$  ratio  $\leq 0.2$  (i.e.  $O_2$ -rich) the  $(1 \times 1)$  surface changes to a

**Fig. 1.10** STM images demonstrating the development of roughness at various stages of CO oxidation. **a** missing-row reconstruction, room temperature, vacuum,  $4.5 \text{ nm} \times 4.5 \text{ nm}$ ,  $V_{bias} = -0.10 \text{ V}$ ,  $I_{tunnel} = 52 \text{ pA}$ ; **b** lifting of the missing-row reconstruction,  $T = 433 \text{ K}$ , 1 bar CO,  $15 \text{ nm} \times 15 \text{ nm}$ ,  $V_{bias} = 0.10 \text{ V}$ ,  $I_{tunnel} = 749 \text{ pA}$ ; **c** flat  $(1 \times 1)$  structure in CO-rich flow,  $T = 433 \text{ K}$ ,  $4.5 \text{ nm} \times 4.5 \text{ nm}$ ,  $V_{bias} = -0.04 \text{ V}$ ,  $I_{tunnel} = 86 \text{ pA}$ ; **d** commensurate  $(1 \times 2)$  structure, observed immediately after switching to a more  $O_2$ -rich gas mixture,  $T = 433 \text{ K}$ ,  $4.5 \text{ nm} \times 4.5 \text{ nm}$ ,  $V_{bias} = -0.04 \text{ V}$ ,  $I_{tunnel} = 86 \text{ pA}$ ; **e** Rough, metallic  $(1 \times 1)$  surface, observed after increasing the CO content of the gas mixture again,  $T = 433 \text{ K}$ ,  $4.5 \text{ nm} \times 4.5 \text{ nm}$ ,  $V_{bias} = 0.08 \text{ V}$ ,  $I_{tunnel} = 1004 \text{ pA}$ . This figure was reprinted from [63] with permission from Elsevier



$(1 \times 2)$  structure. This is shown in Fig. 1.10d. No immediate increase in roughness is observed here, excluding that this structure reflects the formation of the  $(1 \times 2)$  missing-row reconstruction. When a Pt(110) surface switches from the  $(1 \times 1)$  structure to the  $(1 \times 2)$  missing-row reconstruction, the number of Pt atoms present in the top layer is halved. As a result, after the transition, the surface is expected to exhibit an island-and-valley pattern of two height levels. This transition-induced roughness would then decay over time. Prolonged exposure of Pt(110) to an  $O_2$ -rich mixture results in an increase in roughness over time, which is related to catalytic turn-over. This will be discussed in more detail below. The result of this roughening is still present immediately after switching the gas composition to CO-rich conditions. Figure 1.10e shows the rough, metallic  $(1 \times 1)$  surface, characteristic for a CO-rich gas mixture. The roughness of the surface decreases steadily over time to the level of Fig. 1.10c. The increasing roughness under reaction conditions has been observed before on Pt(110) [6], and was attributed to a Mars-van-Krevelen-like reaction mechanism [67]. An essential ingredient in this scenario is that the  $(1 \times 2)$  structure observed under  $O_2$ -rich reaction conditions should be regarded as an ultrathin, epitaxial surface oxide. This has been inferred from the first STM observations [6] and it has been verified by Surface X-Ray Diffraction measurements under similar reaction conditions and accompanying Density Functional Theory calculations [8].

The kinetic results for CO oxidation on Pt(110) are shown in Fig. 1.11. When switching back and forth between CO-rich and  $O_2$ -rich mixtures, broad peaks in the  $CO_2$  production are observed. These peaks are indicative of Langmuir-Hinshelwood kinetics, in which the reactivity is highest when the CO and O surface coverages are equal. Furthermore, we observe that the reactivity of the surface oxide, which is present under  $O_2$ -rich conditions, is higher than the reactivity of the metallic surface, which is present under CO-rich conditions (see details in panels b and c of Fig. 1.11). In addition, narrow spikes (see Fig. 1.11b) are observed just before the Langmuir-Hinshelwood peaks in the  $CO_2$  production, but only when switching from the oxide to the metallic surface. We ascribe these spikes to an increased reaction rate when the CO content above the oxide is raised, and the sudden drop in reaction when the active surface oxide is removed due to high CO supply.

### 1.4.2 CO Oxidation on Pd(100)

CO oxidation on Pd(100) was investigated at a total pressure of 1.25 bar and a temperature of 408 K using the ReactorSTM [61, 62, 68]. Figure 1.12 shows the partial pressures of the reactants (CO and  $O_2$ ) and the product ( $CO_2$ ) (upper panel) and characteristic STM images (lower panel). At  $t = 0$  s the CO pressure was slowly decreased. Image A shows the metallic Pd(100) surface, consisting of flat terraces separated by monoatomic steps. This surface has the same structure as a clean Pd(100) surface imaged in UHV. When decreasing the CO pressure, the  $CO_2$  pressure decreases accordingly. However, at  $t = 1612$  s, a sudden increase in  $CO_2$  production is observed, coinciding with a significant change of the structure of the

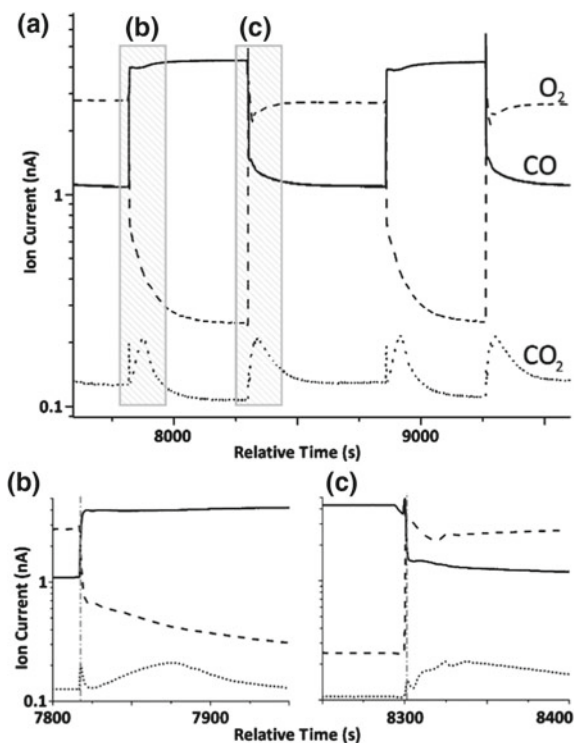


**Fig. 1.11** Semi-logarithmic plot of the reaction kinetics during CO oxidation on Pt (110) at 1 bar and 433 K, measured with a QMS. **a** Two cycles in which the gas composition has been changed back and forth from CO-rich (*solid line*) to O<sub>2</sub>-rich (*dashed line*). The product, CO<sub>2</sub>, (*dotted line*) shows broad peaks during the switching that are indicative of Langmuir-Hinshelwood kinetics. **b** and **c** show zooms of the gray dashed regions. The oxide phase shows higher activity. The spike in **b** indicates the high reaction rate on the oxide during the initial stage of increase of the CO partial pressure, followed by the drop in the rate, when the oxide phase is removed due to the high CO partial pressure. This figure was reprinted from [63] with permission from Elsevier

Pd(100) surface (Image B, top). A large number of clusters is observed, with heights equal to that of a monoatomic step of Pd(100). This formation of clusters is found to accompany the initial stages of Pd(100) oxidation [69]. Therefore, we conclude that in Image B the surface oxidizes to form PdO, and that this causes the observed increase in reactivity. In time, roughness develops and a polycrystalline, granular structure is formed (Images C to E). In this stage, the CO<sub>2</sub> production decreases proportional to the decreasing CO pressure. At  $t = 4700$  s we increase the CO partial pressure again. The Pd smoothens and the flat, metallic surface is restored (Images F and G). With the increase in CO pressure, a modest increase in CO<sub>2</sub> production is observed. At  $t \sim 6700$  s we switch off the O<sub>2</sub> flow and we increase the CO pressure (Image H). Switching from an oxygen-rich to a CO-rich flow, the CO<sub>2</sub> production peaks at  $t = 7010$  s. As the O<sub>2</sub> was pumped out, the CO<sub>2</sub> production steadily

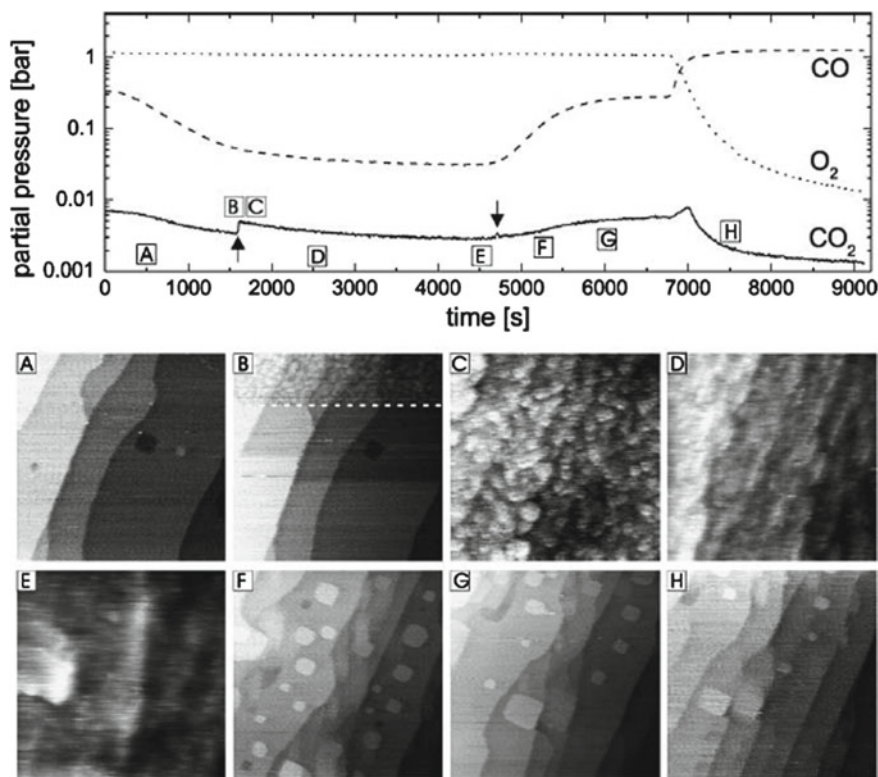


**Fig. 1.12** (Upper panel) Mass spectrometer signals of the reactants (CO and O<sub>2</sub>) and the product (CO<sub>2</sub>) during CO oxidation on the Pd(100) surface at a total pressure of 1.25 bar and a temperature of 408 K. The labels A–H refer to the STM images shown in the lower panel. The arrows mark the changes in reactivity from low to high and vice versa. (Lower panel) STM images (140 nm x 140 nm,  $V_{bias} = 112$  mV,  $I_{tunnel} = 200$  pA) obtained during the CO oxidation reaction. This figure was reprinted from [68] with permission from Elsevier

decreased. When comparing Images G and H, we observe no essential structural changes when switching from a modest to a high ratio between the partial pressures of CO and O<sub>2</sub>.

### 1.4.3 NO Reduction on Pt(110)

The catalytic conversion of nitrogen oxides (NO<sub>x</sub>) is one of the three processes taking place on the three-way car catalyst [64, 65]. The major exhaust pollutants of cars are hydrocarbons, CO, and NO<sub>x</sub>. The NO<sub>x</sub> is formed during the phase of very high temperature (>1500 °C) of the combustion process resulting in thermal fixation of

the nitrogen in air [70]. The exhaust of  $\text{NO}_x$  and hydrocarbons into the air, combined with sun light, results in the formation of ozone, a major component of smog. It was estimated that by the year 2000, over 800 million tons of combined pollutants of hydrocarbons, CO, and  $\text{NO}_x$  have been abated using automotive catalysts [71].

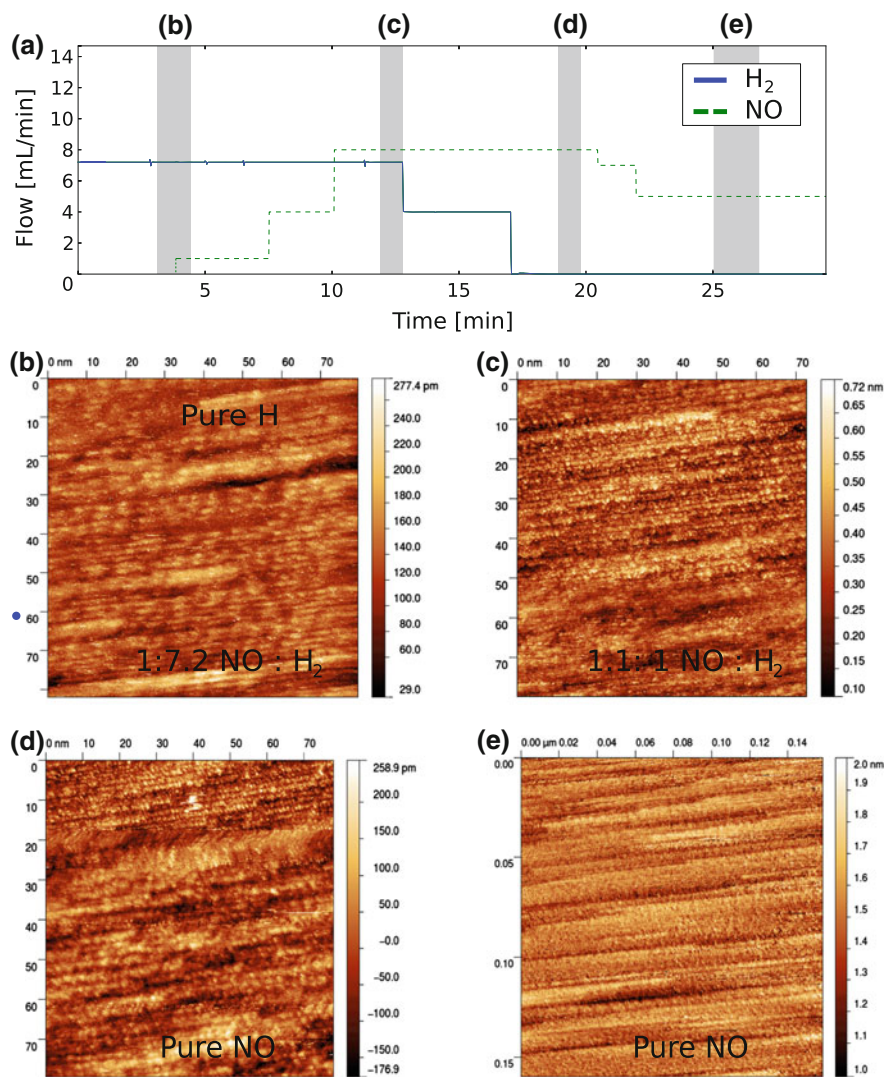
Considering the importance of the NO reduction reaction (either by  $\text{H}_2$  or CO), it is very surprising that almost no *in situ* or *operando* studies have been performed for this system. To the best of our knowledge, the only results for NO reduction on platinum under reaction conditions have been obtained in our group [72]. In this work it was shown that the results for the NO + CO reaction on Pt(100) obtained under high-pressure conditions strongly differ from results obtained in UHV. In the former case, the Pt(100) surface switches between a  $(1 \times 1)$  reconstruction and a quasi-hexagonal structure, depending on the CO/NO ratio at 1.25 bar [72]. Here we discuss the reduction of NO by  $\text{H}_2$  over Pt(110). This reaction is not very selective over Pt, and many products, e.g.  $\text{NH}_3$ ,  $\text{H}_2\text{O}$ ,  $\text{N}_2$ , and  $\text{N}_2\text{O}$ , can be formed.

Figure 1.13 shows the results when exposing the Pt(110) surface to  $\text{H}_2$  and NO. In Fig. 1.13a the gas composition is shown as a function of time. Gray bars show the times at which the STM images were measured. Prolonged exposure to pure  $\text{H}_2$  at room temperature at a pressure of 1.2 bar resulted in a row structure with a  $(1 \times 4)$  periodicity (see Fig. 1.13b). Also, some deeper missing-row features can be observed. Subsequently, this surface has been exposed to NO at increasing NO: $\text{H}_2$  ratios (Fig. 1.13c–e). The blue dot in the first image (b) indicates the switching point from pure  $\text{H}_2$  to a mixture with a NO: $\text{H}_2$  ratio of 1:7.2. Exposure to NO slowly lifts the missing-row reconstruction, leaving flat terraces on the surface.

#### 1.4.4 Fischer-Tropsch Synthesis on Co(0001)

In the Fischer-Tropsch synthesis reaction [73] a mixture of  $\text{H}_2$  and CO (syngas) is converted via a surface polymerization reaction over a cobalt-based catalyst into linear hydrocarbons [74]. Industrial conditions for this reaction include pressures of 1 to several tens of bars, and temperatures between 423 and 573 K. Figure 1.14a shows an STM image obtained in a CO: $\text{H}_2$ :Ar = 1:2:2 mixture at 4 bar and 483 K over Co(0001) [75]. From the image it is clear that under these reaction conditions the surface is completely covered by arrays of stripes, that run parallel to the  $\langle 10\bar{1}0 \rangle$  crystallographic directions of the Co(0001) surface. The stripe pattern exhibits a period of  $1.8 \pm 0.3$  nm, which is the same for the three equivalent orientations and is found everywhere on the surface. The period can be recognized easily in Fig. 1.14b, which is a zoomed-in part of Fig. 1.14a. The stripe pattern is strongly reminiscent of similar patterns reported in the literature for e.g.  $\text{C}_{16}\text{H}_{34}$  on Au(111) [76] and  $\text{C}_{14}\text{H}_{30}$  on highly-oriented pyrolytic graphite (HOPG) [77]. These hydrocarbon molecules self-assemble into regular, striped patterns. We therefore interpret the striped pattern observed in our experiments as hydrocarbon molecules synthesized in the Fischer-Tropsch reaction that lie flat on the Co(0001) surface. The period of the stripes  $L$





**Fig. 1.13** Gas composition as a function of time and *in situ* STM images during NO reduction on Pt(110) at a total pressure of 1.2 bar and room temperature. **a** stepwise change from  $\text{H}_2$  (blue) to  $\text{NO}$  (green) at room temperature and a total pressure of 1.2 bar. Gray regions indicate at which point in time under what conditions the STM images were obtained; **b** Pure  $\text{H}_2$  followed by a switch to a partial pressure ratio of  $\text{NO}:\text{H}_2 = 1:7.2$ ,  $80 \text{ nm} \times 82 \text{ nm}$ ,  $V_{\text{bias}} = -0.70 \text{ V}$ ,  $I_{\text{tunnel}} = 139 \text{ pA}$ ; **c** Pt(110) at a partial pressure ratio  $\text{NO}:\text{H}_2 = 1.1 : 1.0$ ,  $73 \text{ nm} \times 80 \text{ nm}$ ,  $V_{\text{bias}} = -0.70 \text{ V}$ ,  $I_{\text{tunnel}} = 141 \text{ pA}$ ; **d** pure  $\text{NO}$  atmosphere,  $78 \text{ nm} \times 80 \text{ nm}$ ,  $V_{\text{bias}} = -0.70 \text{ V}$ ,  $I_{\text{tunnel}} = 141 \text{ pA}$ ; **e** after prolonged  $\text{NO}$  exposure,  $158 \text{ nm} \times 160 \text{ nm}$ ,  $V_{\text{bias}} = -0.70 \text{ V}$ ,  $I_{\text{tunnel}} = 139 \text{ pA}$ . This figure was reprinted from [63] with permission from Elsevier

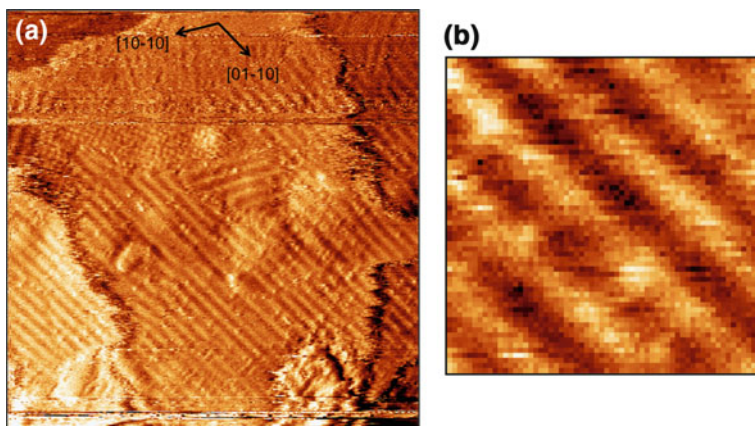


**Fig. 1.14** STM image of **a** Co(0001) exposed to 4 bar of  $\text{CO:H}_2\text{:Ar} = 1:2:2$  at 483 K,  $62 \text{ nm} \times 62 \text{ nm}$ ; **b** enlarged view of part of (a),  $7.5 \text{ nm} \times 7.5 \text{ nm}$ .  $V_{\text{bias}} = 0.3 \text{ V}$ ,  $I_{\text{tunnel}} = 100 \text{ pA}$

is directly related to the molecular length  $l_n$  of a linear hydrocarbon with  $n$  carbon atoms [78, 79]:  $L = l_n = l_0 + n \times l_{\text{CH}_2}$ . Here,  $l_{\text{CH}_2}$  stands for the length of a  $\text{CH}_2$  unit and  $l_0$  is a length offset that takes into account the two methyl end groups of the hydrocarbon chains and the distance between the molecules that face each other in neighboring stripes. The observed stripe period corresponds to a molecular chain length of  $14 \pm 2 \text{ C atoms}$ .

We attribute the emergence of a well-defined period to the combination of three processes that take place on the surface. The first process is the formation of hydrocarbons on the surface via a chain growth mechanism:  $\text{H}_2$  and  $\text{CO}$  dissociate on the Co(0001) surface, and react to form hydrocarbons and water. The length of the hydrocarbons formed is a linear function of time: At each length, there is a constant probability for the chain growth process to continue, while the alternative is for the molecule to detach from the active site (step), at which point the chain stops growing. This scenario leads to an exponential distribution of produced chain lengths, which is dominated very strongly by the shorter chains. The second process is the thermally activated desorption of the hydrocarbons from the cobalt surface. When we assume the desorption energy to be proportional to the chain length, the short molecules stay on the surface for a very short time, while the longer ones tend to slowly accumulate. Finally, the third process is the condensation of the accumulating molecules into well-ordered, two-dimensional islands. This will happen when the surface is populated sufficiently strongly with molecules. The first molecular length that reaches the condensation level defines the stripe period. Shorter molecules do not reach a sufficiently high coverage, while longer molecules could in principle accumulate even more strongly, but would do so at such a late stage, that by then the surface is already saturated with a full molecular monolayer. Model calculations confirm this mechanism and show that a relatively long molecular chain length in the

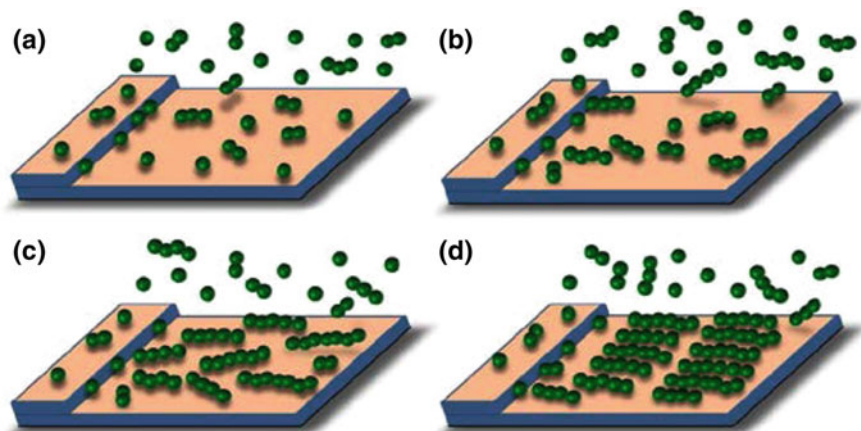


**Fig. 1.15** Schematic scenario for the formation of the striped alkane phase on Co(0001) during the early stages of FT synthesis. The cobalt surface is shown as two terraces, separated by a monoatomic step. For the hydrocarbon chains, only the C atoms are depicted, as *green balls*. **a, b** Formation of monomers, dimers, and longer linear chains, growing from the step sites. **c, d** Desorption of the shorter chains from the surface and accumulation of longer chains on the cobalt terraces

order of 14 C atoms should indeed be expected. This process is qualitatively depicted in Fig. 1.15 [75].

### 1.4.5 Hydrodesulfurization Reaction

Hydrodesulfurization is the treatment of fossil fuels to remove sulfur-containing compounds from crude oil. Due to the stringent requirements for ultralow sulfur fuels, the interest in the catalytic hydrodesulfurization (HDS) process has grown. The industrial catalyst for HDS consists of alumina-supported  $\text{MoS}_2$  nanoparticles. These nanoparticles are formed via sulfidation of  $\text{MoO}_3$  nanoparticles. The active phase is generally accepted to be present as a few nm-wide, single-layer,  $\text{MoS}_2$ -like nanoparticles, usually promoted with Co or Ni [80]. The HDS activity has been attributed to sites at the edges of  $\text{MoS}_2$  clusters, where S atoms are stripped off by  $\text{H}_2$ , creating sulfur vacancies. These vacancies are believed to have a high affinity for binding the sulfur-containing fuel molecules, thereby facilitating the sulfur extraction. Some of the basic steps in this process have been recognized in STM images obtained under UHV conditions (see e.g. [81–83]). Here we show the first STM results for HDS obtained under high-pressure conditions.

Figure 1.16a shows an STM image taken in UHV of  $\text{MoS}_2$  nanoparticles grown on a Au(111) substrate, the model catalyst for HDS in our studies. As can be clearly seen, the  $\text{MoS}_2$  particles form triangular shapes, truncated triangles, and hexagonal shapes, in agreement with previous literature, see e.g. [83–85]. In previous



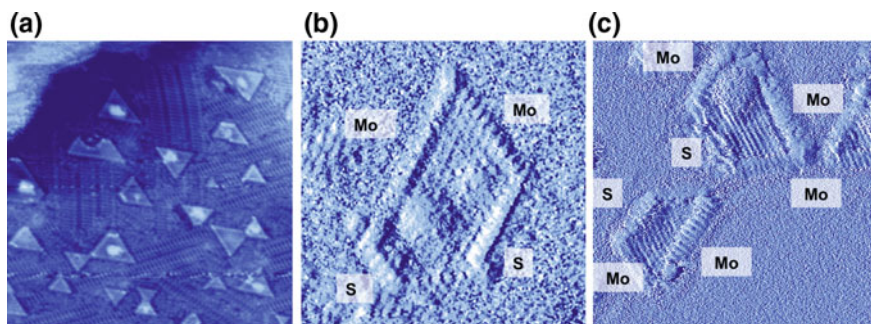


**Fig. 1.16** **a** STM image taken in UHV of  $\text{MoS}_2$  nanoparticles grown on a Au(111) substrate,  $32 \text{ nm} \times 32 \text{ nm}$ ,  $V_{\text{bias}} = -0.30 \text{ V}$ ,  $I_{\text{tunnel}} = 340 \text{ pA}$ ; **b** STM image of  $\text{MoS}_2/\text{Au}(111)$  taken in 1 bar  $\text{H}_2$  at 326 K,  $7.5 \text{ nm} \times 7.5 \text{ nm}$ ,  $V_{\text{bias}} = -0.30 \text{ V}$ ,  $I_{\text{tunnel}} = 675 \text{ pA}$ ; **c** STM image of  $\text{MoS}_2/\text{Au}(111)$  taken under HDS reaction conditions: 1 bar 90%  $\text{H}_2$ , 10%  $\text{CH}_3\text{SH}$  at 523 K,  $7.5 \text{ nm} \times 7.5 \text{ nm}$ ,  $V_{\text{bias}} = -0.30 \text{ V}$ ,  $I_{\text{tunnel}} = 675 \text{ pA}$ . Images **b** and **c** are shown in derivative mode, to enhance contrast

UHV studies, it was found that the nanoparticles can have different structures at their edges [84]. Hexagonal nanoparticles will have edge terminations consisting of  $(10\bar{1}0)$  Mo edges and  $(\bar{1}010)$  S edges. The Mo edges are considered to be the most dominant sites and the active sites for the HDS reaction. Under reaction conditions, these Mo sites can have different coverages of S, which can be observed from the orientation of the edge atoms with respect to the atoms in the basal plane of the particle. When the Mo edge is fully covered with S, i.e. the 100% S-Mo edge, the atoms in the edge sites are out of registry with the atoms in the basal plane [84]. When a 50% S coverage is present, the Mo atoms in the edge are in registry with the Mo atoms in the basal plane of the particle.

When exposing the  $\text{MoS}_2$  nanoparticles to 1 bar of  $\text{H}_2$  at slightly elevated temperature (326 K), the nanoparticles form predominantly hexagonal shapes, as seen in Fig. 1.16b. In the image the presence of both Mo edges and S edges in one nanoparticle can be observed. From the registry of the edge Mo atoms with respect to the atoms in the basal plane, we conclude that we are observing a 50% S-Mo edge here. When exposing the  $\text{MoS}_2$  nanoparticles to HDS conditions (90%  $\text{H}_2$ , 10%  $\text{CH}_3\text{SH}$  at 1 bar and 523 K), see Fig. 1.16c, we observe hexagonal nanoparticles. The particles have both S and Mo edges. The top two particles in Fig. 1.16c show 50% S-Mo edges, while the bottom particle shows 100% S-Mo edges.

#### 1.4.6 Deacon Process for Chlorine Production

Chlorine is one of the most important compounds produced in the chemical industry. Its worldwide annual production is approximately 50 megaton, and it is responsible for approximately 50% of the total turnover of the chemical industry [86]. It is usually produced from HCl or chloride salts. The production method of choice

is presently electrochemical reduction of these reactants, but this is highly energy demanding and it generates large quantities of  $\text{CO}_2$ . Due to these high economical costs and undesired effects for the environment, interest is growing in the heterogeneously catalyzed oxidation of  $\text{HCl}$ , the so-called Deacon process [87, 88]. Sumitomo Chemicals claims that the Deacon process can reduce the power consumption from 1100 kwh to 165 kwh per ton  $\text{Cl}_2$  produced [89].

Several catalysts have been developed for the industrial Deacon process. Examples are  $\text{CuCl}_2$  [87, 88],  $\text{CuCl}_2\text{-KCl/SiO}_2$  [90, 91],  $\text{Cr}_2\text{O}_3\text{/SiO}_2$  [92–94],  $\text{RuO}_2\text{/TiO}_2$  [89, 95], and  $\text{RuO}_2\text{/SnO}_2$  [96–98]. All these catalysts have been employed with varying degrees of success. Severe problems are loss of catalytic activity due to volatilization of the active phase, sintering of active sites and supports, and corrosion issues due to the combined presence of  $\text{HCl}$  and  $\text{H}_2\text{O}$ . At the moment, the catalysts employed in the industry (i.e. Sumitomo Chemicals and Covestro) are based on  $\text{RuO}_2$ . To obtain fundamental insight in the delicate interplay between the atomic-scale structure, the reaction mechanisms, and the performance of the catalyst, we are currently investigating its behavior under relevant conditions of high pressure and high temperature. Here we present some first results and we discuss the experimental issues of this highly aggressive system.

Figure 1.17a, b shows STM images of the  $\text{RuO}_2(110)\text{/Ru}(0001)$  model catalyst obtained under UHV conditions. The images show rectangular-shaped terraces (a) and vaguely visible oxide rows (b), well-known for this surface [5, 99]. Upon exposure to the reaction mixture (1 bar of  $\text{HCl}:\text{O}_2 = 1:4$ ) at room temperature (Fig. 1.17c), holes appear in the surface, due to etching by  $\text{HCl}$ . At this temperature, it seems that no re-oxidation of the film occurs when switching to 1 bar of  $\text{O}_2$ . Within the sensitivity limits of our QMS, no production of  $\text{Cl}_2$  is observed at room temperature. X-ray photoelectron spectra taken after the reaction, however, show the presence of  $\text{Cl}$  on the surface.

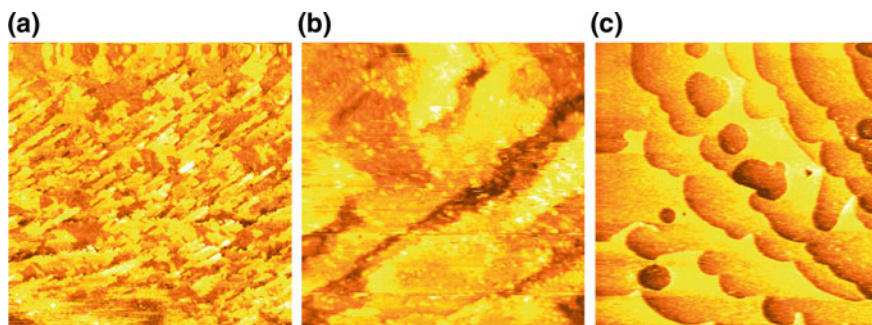


**Fig. 1.17** **a** STM image of a  $\text{RuO}_2(110)$  film on  $\text{Ru}(0001)$  under UHV conditions at room temperature,  $400\text{ nm} \times 400\text{ nm}$ ,  $V_{\text{bias}} = 3.0\text{ V}$ ,  $I_{\text{tunnel}} = 300\text{ pA}$ ; **b** STM image of a  $\text{RuO}_2(110)$  film on  $\text{Ru}(0001)$  under UHV conditions at room temperature,  $50\text{ nm} \times 50\text{ nm}$ ,  $V_{\text{bias}} = 3.0\text{ V}$ ,  $I_{\text{tunnel}} = 250\text{ pA}$ ; **c** STM image of a  $\text{RuO}_2(110)$  film on  $\text{Ru}(0001)$  during exposure to 1 bar of  $\text{HCl}:\text{O}_2 = 1:4$  at room temperature,  $800\text{ nm} \times 800\text{ nm}$ ,  $V_{\text{bias}} = 2.75\text{ V}$ ,  $I_{\text{tunnel}} = 100\text{ pA}$

With these first images we have shown that our set-up is capable of dealing with these very aggressive reaction conditions. However, some experimental issues were observed and have been dealt with. These include corrosion of the W tip (we now switched to PtIr), corrosion of the Cu seal in the leak valve of the QMS chamber (we now switched to a teflon-type seal), and decomposition of the Kalrez seal due to the combination of elevated temperatures and corrosive gases.

## 1.5 Conclusions and Outlook

Using the ReactorSTM and ReactorAFM we are able to cast a direct view on catalyst surfaces under industrially relevant conditions of high pressure and temperature. The ReactorSTM is now in a sufficiently mature state that reactions more complicated than CO oxidation can be studied. As is clear from the examples discussed here, we find pressure gaps for most reaction systems, simply by observing surface structures under reaction conditions that have been observed never before in UHV. The effect of the high pressure is to thermodynamically or kinetically stabilize new surface structures and compositions that incorporate one or more of the reactants. These observations show that a catalyst is more than a mere spectator in chemical reactions: It actively participates! The first results for aggressive chemical reactions, such as hydrodesulfurization and chlorine production, have given us confidence that the instruments described in this Chapter are able to perform under extremely corrosive conditions, showing no signs of degradation or destruction. Preliminary experiments using the ReactorAFM have shown that we can perform *in situ* studies of non-conducting surfaces under reaction conditions. With the promise of this instrument enabling us to obtain atomic-scale images of metallic nanoparticles supported on oxidic, insulating surfaces, we will be able in the near future to also bridge the materials gap.

**Acknowledgements** The work described in this chapter would not have been possible without the contributions of many people. The authors would like to thank Rik Mom, Violeta Navarro, Willem Onderwaater, Sander Roobol, Matthijs van Spronsen, Johan Bakker, Mirthe Bergman, Stefania Bobaru, Marta Cañas-Ventura, Bas Hendriksen, Kees Herbschleb, Qian Liu, Peter Rasmussen, Marcel Rost, and Dunja Stolz. The authors are indebted to the fine-mechanical department of Leiden University, and especially to Peter van der Tuijn, who was vital for the design of the latest version of the ReactorSTM and the ReactorAFM. We owe a special thanks to Gertjan van Baarle and Alexei Ofitserov of Leiden Probe Microscopy B.V., who participated in the design of the prototypes of the Reactor set-ups and developed the commercial version of the ReactorSTM. This work is financially supported by NanoNextNL, a micro- and nanotechnology consortium of the Government of the Netherlands and 130 partners, and by a SmartMix grant and the NIMIC partner organizations through NIMIC, a public-private program. IMNG acknowledges the support of STW, which is financially supported by the Netherlands Organization for Scientific Research (NWO), through a Veni grant.

## References

1. J. Wintterlin, *Adv. Catal.* **45**, 131 (2000)
2. P. Stoltze, J.K. Nørskov, *Phys. Rev. Lett.* **55**, 2502 (1985)
3. J.A. Rodriguez, D.W. Goodman, *Surf. Sci. Rep.* **14**, 1 (1991)
4. X. Su, P.S. Cremer, Y.R. Shen, G.A. Somorjai, *J. Am. Chem. Soc.* **119**, 3994 (1997)
5. H. Over, Y.D. Kim, A.P. Seitsonen, S. Wendt, E. Lundgren, M. Schmid, P. Varga, A. Morgante, G. Ertl, *Science* **287**, 1474 (2000)
6. B.L.M. Hendriksen, J.W.M. Frenken, *Phys. Rev. Lett.* **89**, 046101 (2002)
7. H. Over, M. Muhler, *Prog. Surf. Sci.* **72**, 3 (2003)
8. M.D. Ackermann, T.M. Pedersen, B.L.M. Hendriksen, O. Robach, S.C. Bobaru, I. Popa, C. Quirós, H. Kim, B. Hammer, S. Ferrer, J.W.M. Frenken, *Phys. Rev. Lett.* **95**, 25505 (2005)
9. R. Westerström, J. Gustafson, A. Resta, A. Mikkelsen, J.N. Andersen, E. Lundgren, N. Seriani, F. Mittendorfer, M. Schmid, J. Kikiovits, P. Varga, M.D. Ackermann, J.W.M. Frenken, N. Kasper, A. Stierle, *Phys. Rev. B* **76**, 155410 (2007)
10. H. Bluhm, M. Hävecker, A. Knop-Gericke, M. Kiskinova, R. Schlögl, M. Salmeron, *MRS Bull.* **32**, 1022 (2007)
11. M. Salmeron, R. Schlögl, *Surf. Sci. Rep.* **63**, 169 (2008)
12. W.P.A. Jansen, A.W.D. van der Gon, G.M. Wijers, Y.G.M. Rikers, H.H. Brongersma, P.W. van der Hoogen, J.A.M. de Laat, T.M. Maas, E.C.A. Dekkers, P. Brinkgreve, *Rev. Sci. Instrum.* **73**, 354 (2002)
13. P.L. Hansen, J.B. Wagner, S. Helveg, J.R. Rostrup-Nielsen, B.S. Clausen, H. Topsøe, *Science* **295**, 2053 (2002)
14. P.L. Gai, E.D. Boyes, S. Helveg, P.L. Hansen, S. Giorgio, C. Henry, *MRS Bull.* **32**, 1044 (2007)
15. J.F. Creemer, S. Helveg, G.H. Hovelings, S. Ullmann, A.M. Molenbroek, P.M. Sarro, H.W. Zandbergen, *Ultramicroscopy* **108**, 993 (2008)
16. E. de Smit, I. Swart, J.F. Creemer, G.H. Hovelings, M.K. Gilles, T. Tyliszczak, P.J. Kooyman, H.W. Zandbergen, C. Morin, B.M. Weckhuysen, F.M.F. de Groot, *Nature* **456**, 222 (2008)
17. P.B. Rasmussen, B.L.M. Hendriksen, H. Zeijlemaker, H.G. Ficke, J.W.M. Frenken, *Rev. Sci. Instrum.* **69**, 3879 (1998)
18. B.L. Weeks, C. Durkan, H. Kuramochi, M.E. Welland, T. Rayment, *Rev. Sci. Instrum.* **71**, 3777 (2000)
19. F. Tao, D. Tang, M. Salmeron, G.A. Somorjai, *Rev. Sci. Instrum.* **79**, 084101 (2008)
20. C.T. Herbschleb, P.C. van der Tuijn, S.B. Roobol, V. Navarro, J.W. Bakker, Q. Liu, D. Stoltz, M.E. Cañas-Ventura, G. Verdoes, M.A. van Spronsen, M. Bergman, L. Crama, I. Taminiau, A. Ofitserov, G.J.C. van Baarle, J.W.M. Frenken, *Rev. Sci. Instrum.* **85**, 083703 (2014)
21. S.B. Roobol, M.E. Cañas-Ventura, M. Bergman, M.A. van Spronsen, W.G. Onderwaater, P.C. van der Tuijn, R. Koehler, A. Ofitserov, G.J.C. van Baarle, J.W.M. Frenken, *Rev. Sci. Instrum.* **86**, 033706 (2015)
22. X. Su, P.S. Cremer, Y.R. Shen, G.A. Somorjai, *Phys. Rev. Lett.* **77**, 3858 (1996)
23. G. Rupprechter, T. Dellwig, H. Unterhalt, H.-J. Freund, *J. Phys. Chem. B* **105**, 3797 (2001)
24. G. Rupprechter, *MRS Bull.* **32**, 1031 (2007)
25. G.A. Beitel, A. Laskov, H. Oosterbeek, E.W. Kuipers, *J. Phys. Chem* **100**, 12494 (1996)
26. C. Li, P.C. Stair, *Catal. Lett.* **36**, 119 (1996)
27. P.C. Stair, C. Li, *J. Vac. Sci. Technol. A* **15**, 1679 (1997)
28. C. Li, P.C. Stair, *Catal. Today* **33**, 353 (1997)
29. H.H. Rotermund, *Surf. Sci.* **386**, 10 (1997)
30. H. Isern, K. Peters, P. Steadman, O. Robach, J. Alvarez, E. Lundgren, S. Ferrer, *Surf. Sci.* **482–485**, 101 (2001)
31. S. Ferrer, M.D. Ackermann, E. Lundgren, *MRS Bull.* **32**, 1010 (2007)
32. R. van Rijn, M.D. Ackermann, O. Balmes, T. Dufrane, A. Geluk, H. Gonzalez, H. Isern, E. de Kuiper, L. Petit, V.A. Sole, D. Wermeile, R. Felici, J.W.M. Frenken, *Rev. Sci. Instrum.* **81**, 014101 (2010)

33. A. Knop-Gericke, M. Hävecker, T. Schedel-Niedrig, R. Schlögl, *Catal. Lett.* **66**, 215 (2000)
34. J. Evans, A. Puig-Molina, M. Tromp, *MRS Bull.* **32**, 1038 (2007)
35. C.J. Chen, *Introduction to Scanning Tunneling Microscopy* (Oxford University Press, Oxford, 1993)
36. L. Kuipers, R.W.M. Loos, H. Neerings, J. ter Horst, G.J. Ruwiel, A.P. de Jongh, J.W.M. Frenken, *Rev. Sci. Instrum.* **66**, 4557 (1995)
37. M.S. Hoogeman, D.G. van Loon, R.W.M. Loos, H.G. Ficke, E. de Haas, J.J. van der Linden, H. Zeijlemaker, L. Kuipers, M.F. Chang, M.A.J. Klik, J.W.M. Frenken, *Rev. Sci. Instrum.* **69**, 2072 (1998)
38. G. Binnig, H. Rohrer, *Helv. Phys. Acta.* **55**, 726 (1982)
39. G. Binnig, H. Rohrer, *Rev. Mod. Phys.* **56**, 615 (1987)
40. G. Binnig, H. Rohrer, C. Gerber, E. Weibel, *Appl. Phys. Lett.* **40**, 178 (1982)
41. G. Binnig, H. Rohrer, C. Gerber, E. Weibel, *Phys. Rev. Lett.* **49**, 57 (1982)
42. R. Wiesendanger, *Scanning Probe Microscopy and Spectroscopy* (Cambridge University Press, Cambridge, 1994)
43. B.J. McIntyre, M. Salmeron, G.A. Somorjai, *Rev. Sci. Instrum.* **64**, 687 (1993)
44. J.A. Jensen, K.B. Rider, Y. Chen, M. Salmeron, G.A. Somorjai, *J. Vac. Sci. Technol. B* **17**, 1080 (1999)
45. E. Laegsgaard, L. Österlund, P. Thosttrup, P.B. Rasmussen, I. Stensgaard, F. Besenbacher, *Rev. Sci. Instrum.* **72**, 3537 (2001)
46. A. Kolmakov, D.W. Goodman, *Rev. Sci. Instrum.* **74**, 2444 (2003)
47. M. Rössler, P. Geng, J. Winterlin, *Rev. Sci. Instrum.* **76**, 023705 (2005)
48. F. Tao, L. Nguyen, S. Zhang, *Rev. Sci. Instrum.* **84**, 034101 (2013)
49. J. Lievonen, K. Ranttila, M. Ahlskog, *Rev. Sci. Instrum.* **78**, 043703 (2007)
50. D. D'Agostino, D. Jay, H. McNally, *Microsc. Microanal.* **16**, 1042 (2010)
51. S.R. Higgins, C.M. Eggleston, K.G. Knauss, C.O. Boro, *Rev. Sci. Instrum.* **69**, 2994 (1998)
52. A.S. Lea, S.R. Higgins, K.G. Knauss, K.M. Rosso, *Rev. Sci. Instrum.* **82**, 043709 (2011)
53. G. Dong, E.B. Fourré, F.C. Tabak, J.W.M. Frenken, *Phys. Rev. Lett.* **104**, 096102 (2010)
54. M. Rost, L. Crama, P. Schakel, E. van Tol, G. van Velzen-Williams, C. Overgauw, H. ter Horst, H. Dekker, B. Okhuijsen, M. Seynen, A. Vijftigschild, P. Han, A.J. Katan, K. Schoots, R. Schumm, W. van Loo, T.H. Oosterkamp, J.W.M. Frenken, *Rev. Sci. Instrum.* **76**, 053710 (2005)
55. F.J. Giessibl, S. Hembacher, H. Bielefeldt, *Science* **289**, 422 (2000)
56. L. Gross, F. Mohn, N. Moll, P. Liljeroth, G. Meyer, *Science* **325**, 1110 (2009)
57. F.J. Giessibl, *Appl. Phys. Lett.* **73**, 3956 (1998)
58. A. Botman, M. Hesselberth, J.J.L. Mulders, *Microelectron. Eng.* **85**, 1139 (2008)
59. R. Grober, J. Acimovic, J. Schuck, D. Hessman, P.J. Kindlemann, J. Hespanha, A.S. Morse, *Rev. Sci. Instrum.* **71**, 2776 (2000)
60. Leiden Probe Microscopy B.V. <http://www.leidenprobemicroscopy.com/>
61. B.L.M. Hendriksen, S.C. Bobaru, J.W.M. Frenken, *Catal. Today* **105**, 234 (2005)
62. B.L.M. Hendriksen, S.C. Bobaru, J.W.M. Frenken, *Top. Catal.* **36**, 43 (2005)
63. M.A. van Spronsen, G.J.C. van Baarle, C.T. Herbschleb, J.W.M. Frenken, I.M.N. Groot, *Catal. Today* **244**, 85 (2015)
64. R.M. Heck, R.J. Farrauto, *Appl. Catal. A: General* **221**, 443 (2001)
65. M. Shelef, *Catal. Rev. Sci. Eng.* **11**, 1 (1975)
66. E. Vlieg, I.K. Robinson, K. Kern, *Surf. Sci.* **233**, 248 (1990)
67. P. Mars, D.W. van Krevelen, *Chem. Eng. Sci.* **3**, 41 (1954)
68. B.L.M. Hendriksen, S.C. Bobaru, J.W.M. Frenken, *Surf. Sci.* **552**, 229 (2004)
69. G. Zheng, E.I. Altman, *Surf. Sci.* **504**, 253 (2002)
70. J. Zeldovich, *Acta Phys. USSR* **21**, 577 (1946)
71. R.M. Heck, R.J. Farrauto, *Automotive Engineering* February p. 93 (1996)
72. C.T. Herbschleb, S.C. Bobaru, J.W.M. Frenken, *Catal. Today* **154**, 61 (2010)
73. F. Fischer, H. Tropsch, *Brennst. Chem.* **7**, 97 (1926)
74. D. Leckel, *Energy Fuels* **23**, 2342 (2009)

75. V. Navarro, M.A. van Spronsen, J.W.M. Frenken, *Nat. Chem.* **8**, 929 (2016)
76. J. Cousty, A. Marchenko, *Surf. Sci.* **520**, 128 (2002)
77. Q. Chen, H.-J. Yan, C.-J. Yan, G.-B. Pan, L.-J. Wan, G.-Y. Wen, D.-Q. Zhang, *Surf. Sci.* **602**, 1256 (2008)
78. J. Marchenko, A. Cousty, *Surf. Sci.* **520**, 128 (2002)
79. K. Uosaki, R. Yamada, *J. Am. Chem. Soc.* **121**, 4090 (1999)
80. H. Topsøe, B.S. Clausen, F.E. Massoth, *Hydrotreating Catalysis, Science and Technology* (Springer Verlag, Berlin, 1996)
81. S. Helveg, J.V. Lauritsen, E. Laegsgaard, I. Stensgaard, J.K. Nørskov, B.S. Clausen, H. Topsøe, F. Besenbacher, *Phys. Rev. Lett.* **84**, 951 (2000)
82. J.V. Lauritsen, S. Helveg, E. Laegsgaard, I. Stensgaard, B.S. Clausen, H. Topsøe, F. Besenbacher, *J. Catal.* **197**, 1 (2001)
83. J.V. Lauritsen, M.V. Bollinger, E. Laegsgaard, K.W. Jacobsen, J.K. Nørskov, B.S. Clausen, H. Topsøe, F. Besenbacher, *J. Catal.* **221**, 510 (2004)
84. A.S. Walton, J.V. Lauritsen, H. Topsøe, F. Besenbacher, *J. Catal.* **308**, 306 (2013)
85. A. Tuxen, J. Kibsgaard, H. Gobel, E. Laegsgaard, H. Topsøe, J.V. Lauritsen, F. Besenbacher, *ACS Nano* **4**, 4677 (2010)
86. Eurochlor, Chlorine Industry Review (2007–2008)
87. H. Deacon, U.S. Patent **85370** (1868)
88. H. Deacon, U.S. Patent **165802** (1875)
89. K. Iwanaga, K. Seki, T. Hibi, K. Issoh, T. Suzuta, M. Nakada, Y. Mori, T. Abe, *Sumitomo Kagaku* **2004-I** (2004)
90. A.J. Johnson, A.J. Cherniavsky, U.S. Patent **2542961** (1951)
91. S.O. Company, U.S. Patent **3210158** (1965)
92. T. Kiyoura, N. Fujimoto, M. Ajioka, T. Suzuki, Y. Kogure, K. Kanaya, T. Nagayama, European Patent **EP184413A** (1984)
93. H. Itoh, Y. Kono, M. Ajioka, S. Takenaka, M. Kataita, U.S. Patent **4803065** (1989)
94. T. Kiyoura, Y. Kogure, T. Nagayama, K. Kanaya, U.S. Patent **4822589** (1989)
95. T. Hibi, H. Nishida, H. Abekawa, U.S. Patent **5871707** (1999)
96. A. Wolf, L. Mleczko, O. F. Schlüter, S. Schubert, European Patent **EP2026905** (2006)
97. A. Wolf, J. Kintrup, O.F. Schlüter, L. Mleczko, European Patent **EP2027062** (2006)
98. A. Wolf, L. Mleczko, S. Schubert, O.F. Schlüter, European Patent **EP2027063** (2006)
99. M. Rössler, S. Günther, J. Wintterlin, *J. Phys. Chem. C* **111**, 2242 (2007)



Operando Research in Heterogeneous Catalysis

Frenken, J.; Groot, I. (Eds.)

2017, XIV, 222 p. 101 illus., 59 illus. in color., Hardcover

ISBN: 978-3-319-44437-6